Characterization and validation of GNSS multipath-induced Doppler measurement error

Jingxiaotao Fang
Liyuan Zhang
Guohao Zhang
Bing Xu, Member, IEEE
Li-Ta Hsu, Senior Member, IEEE
The Hong Kong Polytechnic University, HK

***Abstract*— Global Navigation Satellite System (GNSS) receivers operating in urban environments frequently encounter multipath interference, a phenomenon wherein direct and reflected signals interact. The Doppler frequency estimation by the GNSS receiver holds critical significance for precise signal synchronization and plays a pivotal role in user velocity estimation. However, a notable research gap exists concerning the multipath effects on the receiver frequency-locked loop (FLL). Therefore, this paper provides a quantitative characterization of the receiver Doppler frequency measurement error in urban areas. A realistic receiver FLL simulator, integrating the ray-tracing at the base-band signal processing level, is introduced to simulate the continuous feedback tracking performance under multipath interference. Real experiments are conducted in urban areas for the validation of theoretical findings and the simulator's reliability. An 81% simulation similarity can be attained. Consequently, the Doppler frequency and velocity measurement errors are quantified by considering factors such as the signal ray parameters, tracking loop architecture, and user dynamics.**

***Index Terms*—Multipath, GNSS simulator, frequency-locked loop, Doppler, ray-tracing, urban environment**

Manuscript received XXXXX 00, 0000; revised XXXXX 00, 0000; accepted XXXXX 00, 0000.
This work was supported in part by the National Natural Science Foundation of China (NSFC) under Grant 62103346, in part by the Guangdong Basic and Applied Basic Research Foundation under Project 2022A1515011680, and in part by the University Grants Committee of Hong Kong under the scheme Research Impact Fund on the project R5009- 21, entitled Reliable Multiagent Collaborative Global Navigation Satellite System Positioning for Intelligent Transportation Systems.

Jingxiaotao Fang is with The Hong Kong Polytechnic University, HK (e-mail: jingxiaotao2.fang@connect.polyu.hk); Liyuan Zhang is with The Hong Kong Polytechnic University, HK (e-mail: liyuen.zhang@connect.polyu.hk); Guohao Zhang is with The Hong Kong Polytechnic University, HK (e-mail: gh.zhang@polyu.edu.hk); Bing Xu is with The Hong Kong Polytechnic University, HK (e-mail: pbing.xu@polyu.edu.hk); Li-Ta Hsu is with The Hong Kong Polytechnic University, HK (e-mail: lt.hsu@polyu.edu.hk). *(Corresponding author: Bing Xu).*

I. INTRODUCTION

In urban areas, multipath interference stands as one of the prominent sources of error in high-precision applications of the Global Navigation Satellite System (GNSS). Multipath signals are a composite of the desired line-of-sight (LOS) or simply direct signal and an undesired reflected signal [1, 2]. The reflected signal, delayed due to interactions with obstacles along its propagation path, reaches the GNSS receiver with shifted synchronization parameters, such as the code phase, carrier phase, and carrier Doppler frequency. Consequently, the interaction of synchronization parameters from the multipath signals may confound the receiver and influence the GNSS receiver navigation solution accuracy. Many researchers have made progress in understanding the impact of multipath on code tracking, establishing theoretical pseudo-range error envelopes, and enabling an assessment of worst-case performance scenarios [3, 4, 5]. In the receiver tracking loops, the carrier Doppler frequency plays a pivotal role in achieving accurate signal synchronization and may exert a considerable impact on the code tracking performance [6]. In challenging environments, the frequency-lock loop (FLL) can be considered an assisting tool in tracking weak and high-dynamic signals [7]. In addition, the receiver Doppler frequency measurement is primarily used in vehicle velocimetry and adding for instantaneous positioning [8, 9]. Therefore, the Doppler frequency error due to multipath reception deserves further investigation, and a considerable amount of research work has been devoted to the error characterization. The existing body of research can be categorized into two focal areas: the true Doppler frequency and the receiver Doppler frequency measurement.

First, the Doppler frequency of the received signal results from the relative motion between the transmitter and receiver, which can be estimated with knowledge of the signal ray geometries and dynamics of the user and satellite. Numerous studies have reported the existence of the Doppler frequency difference between the reflected signal and the LOS signal, often referring to it as the multipath fading frequency, multipath Doppler shift, or simply fading frequency [10, 11, 12]. To avoid potential confusion, this paper denotes the Doppler frequency difference between the reflected signal and the LOS signal as the *frequency shift of the reflected signal*. Ray-tracing is a powerful technique for estimating possible satellite–reflector–antenna geometries, enabling the Doppler frequency of the received signal to be calculated under various scenarios. For instance, researchers have characterized the frequency shift of the reflected signals in scenarios such as a static receiver [13], varying user velocity [11], and different geometrical relationships between satellite, reflector, and receiver [10]. The statistical distribution of the frequency shift of the reflected signal is discussed, considering various satellite orbit types and user velocities as outlined in [12]. The results from these studies indicate the potential for frequency shifts of the

reflected signal to reach magnitudes in tens of Hertz (Hz) in urban environments. Additionally, it is noted that these shifted signals may not be entirely rejected by the receiver tracking loop. Therefore, the reflected signals may distort the receiver tracking point from the LOS signal and finally result in the degradation of the tracking accuracy, introducing errors in velocimetry, positioning, as well as signal-to-noise measurement [10, 11, 14, 15, 16].

Second, the receiver Doppler frequency measurement is the output from the GNSS receiver during a continuous tracking period, which depends on the synchronization results between the incoming signals and the receiver's local replica in the tracking loop. Therefore, in urban areas, the Doppler frequency measurement error, indicating the Doppler frequency difference between the desired LOS Doppler frequency and receiver-measured Doppler frequency, may escalate due to the intersection of multiple signals. Over the years, researchers have made significant progress in characterizing the GNSS receiver code tracking error in multipath environments. However, a neglectable Doppler frequency error is assumed in the code tracking process. For example, some have assumed that the Doppler frequency of the LOS and reflected signals is approximately the same and that the carrier tracking loop is perfectly tracking the LOS signal [17, 18]. This assumption, however, is only suitable in limited scenarios, such as static-user scenarios, scenarios when the LOS signal power significantly exceeds that of the reflected signal, or scenarios when the user velocity is perpendicular to the signal propagation vector. Furthermore, it is often assumed that the receiver rejects the reflected signals because their frequency shifts so fast that they may be filtered out in the tracking loop [14]. However, the frequency shift of the reflected signal can remain within the bandwidth of the tracking loop for urban applications with slow user dynamics. Additionally, researchers have concluded that when multiple signals are received, the GNSS receiver only tracks the signal with higher power [19]. However, the conclusion, based on the analysis of the period-averaged Doppler frequency (the receiver-measured Doppler frequency over a certain period), may not comprehensively represent the Doppler frequency estimation at a single epoch. Recently, the frequency shift of the reflected signal has been reported to cause noticeable oscillation in the signal power measurement, carrier phase, and frequency discriminators' output [20].

In summary, existing research presents several limitations. First, while the frequency shift of the reflected signal has been verified in the literature of the first category, limited attention has been paid to the field of receiver tracking performance characterization. Second, the prevailing assumptions about neglectable Doppler frequency error may only be applicable in limited practical scenarios. Third, some research may overlook the impact of the noise and the signal amplitude degradation due to the reflected signal on the carrier frequency tracking. Last, visualization and validation of the receiver Doppler frequency measurement error in the urban environment remain inadequate. This gap can be attributed to the complex and evolving nature of urban environments, signal strengths, satellite-reflector-receiver geometry, receiver dynamics, and the architecture of receiver tracking systems in practical applications.

Therefore, the previous work characterized the continuous carrier frequency tracking performance and simulated the mutipath-induced Doppler error, or simply *Doppler multipath error*, based on the theoretical model [21]. This paper extends it with the modeling of Doppler multipath error and noise impact and proposes a realistic ray-tracing-aided carrier tracking simulation algorithm. This simulator quantifies the Doppler multipath error in complex environments, such as various signal strengths, satellite-receiver geometries, and receiver tracking architectures in practical applications. This simulator combines the GNSS measurement-level data prediction with the carrier frequency tracking parameter estimation at the baseband processing level. Ray-tracing is utilized to predict the optical LOS and reflected signal rays with the knowledge of 3-dimensional (3D) building models, satellite ephemeris, and the user position, velocity, and time (PVT) information. Consequently, the GNSS measurement-level data, including the signal strength and Doppler frequency, are updated on each epoch for the simulation of continuous tracking of the compound signals. In addition, this paper concerns the slow dynamic scenario of receivers, where the frequency shift remains within the bandwidth of the tracking loop—a scenario frequently encountered in urban applications.

However, two main challenges exist. The first challenge lies in the practical impossibility of accurately predicting signal propagation paths, reflection points, and signal power at every epoch due to the variety of potential interferences in the real environment. Second, the noise term in the receiver-measured Doppler frequency, which may result from signal propagation and receiver processing, presents a significant challenge to estimation [22, 23]. Therefore, achieving a highly accurate simulation for every epoch is currently unattainable, and the proposed simulator is designed to estimate the possible distribution and the evolution pattern of the Doppler frequency measurement under multipath interference. The contributions of this study are summarized below:

1) A theoretical exploration of FLL-based tracking mechanisms under multipath interference is conducted, encompassing the derivation of a Doppler frequency model that considers multiple signal rays. The theoretical impact of the noise on Doppler measurement errors is derived.
2) A realistic ray-tracing-based Doppler simulator is developed. This simulator estimates the practical performance of the receiver feedback tracking loop in urban areas.
3) The simulated receiver-measured Doppler frequency performance under multipath is validated utilizing real data collected from urban environments.

4) The pseudorange rate error envelope is developed, which provides a quick estimation of receiver Doppler frequency measurement behavior in a given multipath reception scenario. The Doppler multipath error and receiver velocity estimation error are simulated for varying user dynamics scenarios.

II. DOPPLER FREQUENCY MODEL

The Doppler frequency of the incoming signal results from the relative motion between the satellite and the receiver. Fig. 1. illustrates the LOS signal path in the green line and the reflected signal path in the red line. The Doppler frequency of the LOS signal can be written

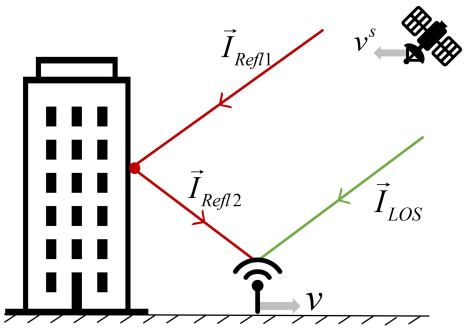

Fig. 1. Illustration of the LOS and reflected signals.

as [1]

$$f_{LOS} = \frac{(v - v^s)\vec{I}_{LOS}}{\lambda} \tag{1}$$

where λ is the GNSS signal carrier wavelength. v and v^s are the receiver and satellite velocities, respectively. $\vec{I}_{LOS}$ is the unit vector pointing towards the LOS signal propagation path. Similarly, the Doppler frequency of the reflected signal from the satellite to the reflector and from the reflector to the user receiver can be expressed as

$$f_{Refl1} = \frac{(0 - v^s)\vec{I}_{Refl1}}{\lambda} \tag{2}$$

$$f_{Refl2} = \frac{(v - 0)\vec{I}_{Refl2}}{\lambda} \tag{3}$$

where $\vec{I}_{Refl1}$ and $\vec{I}_{Refl2}$ represent the unit vectors pointing in alignment with the propagation paths from the satellite to the reflection point and from the reflection point to the receiver, respectively. The reflection point's velocity can be assumed to be zero. Next, the Doppler frequency of the reflected signal transmitted from the satellite to the user receiver can be found as

$$f_{Refl} = f_{Refl1} + f_{Refl2} = \frac{v \cdot \vec{I}_{Refl2} - v^s \cdot \vec{I}_{Refl1}}{\lambda} \tag{4}$$

Therefore, the Doppler difference between the LOS and reflected signals results from the different projections of the receiver velocity onto the signal vectors. In user-static scenarios, the Doppler difference between the LOS and reflected signals could be small because vectors $\vec{I}_{LOS}$ and $\vec{I}_{Refl1}$ are similar due to the large distance between satellite and receiver [13].

III. DOPPLER FREQUENCY ESTIMATION IN RECEIVER TRACKING LOOP

In urban scenarios, it is likely that the signals reflected from the buildings with time delay lie within one code chip length, distorting the receiver tracking point from the correct position. Therefore, this section investigates the GNSS receiver's typical carrier frequency tracking. The following analysis neglects the influence of multiple reflection signals on the Doppler frequency measurement, as the reflected signals arriving at the antenna after multiple reflections are generally too weak [24]. Assume that the received multipath or compound signal consists of one LOS signal and one reflected signal, which can be expressed as [25]

$$\begin{aligned} S(t) = &\sqrt{2C_{LOS}}D(t - \tau_{LOS})x(t - \tau_{LOS})\sin(\omega_{LOS}t + \vartheta_{LOS}) \\ &+ \sqrt{2C_{Refl}}D(t - \tau_{Refl})x(t - \tau_{Refl})\sin(\omega_{Refl}t + \vartheta_{Refl}) \\ &+ v_{IF} \end{aligned} \tag{5}$$

where t represents the sample time. $D(t)$ and $x(t)$ are the navigation data and pseudorandom noise (PRN) code, respectively. C_{LOS} and C_{Refl} are the received power of the LOS and reflected signals, respectively. The square of the signal power $\sqrt{2C_{LOS}}$ and $\sqrt{2C_{Refl}}$ are the amplitudes of the LOS and reflected signals, respectively. The set of $\sqrt{2}$ added to the amplitude is to ease the subsequent manipulation without loss of generality. τ_{LOS}, ω_{LOS} and ϑ_{LOS} are the code phase, angular frequency, and initial carrier phase of the LOS signal, respectively. τ_{Refl}, ω_{Refl} and ϑ_{Refl} are the code phase, angular frequency, and initial carrier phase of the reflected signal, respectively. v_{IF} indicates the intermediate frequency (IF) noise, which is assumed to be additive white Gaussian noise, whose variance is decided by the power spectrum density of the thermal noise.

The incoming IF signal is multiplied by the sine and cosine local replica signals, where the cosine function is supposed to be 90° out of phase with the incoming carrier wave. The local replica's amplitude contains no navigation data due to the unpredictability of the bit transition. For example, the prompt in-phase (I) channel is

$$\begin{aligned} &i_p(t) \\ &= [\sqrt{2C_{LOS}}D(t - \tau_{LOS})x(t - \tau_{LOS})\sin(\omega_{LOS}t + \vartheta_{LOS}) \\ &+ \sqrt{2C_{Refl}}D(t - \tau_{Refl})x(t - \tau_{Refl})\sin(\omega_{Refl}t + \vartheta_{Refl})] \\ &\times \sqrt{2}x(t - \tau_0)\sin(\omega_0 t + \vartheta_0) \end{aligned} \tag{6}$$

where ω_0, ϑ_0 and τ_0 are the carrier angular frequency, initial carrier phase, and code phase of the receiver replica, respectively. The detailed calculation is displayed in Appendix A, and a similar expression can be written to describe the quadra-phase (Q) channel. Note that the correlation output consists of the high-frequency and low-frequency components, whereas the low-frequency component consists of the carrier phase difference between the incoming and local replica signals. Then, the integrate and dump process suppresses the high-frequency component

and noise. After the integrate and dump process, the prompt I- and Q-channel correlation values are shown in (7) and (8) [1]. t_0 is the initial integration time. $R(\cdot)$ is the base-band auto-correlation function (ACF). $\Delta\tau_{LOS} = \tau_{LOS} - \tau_0$ and $\Delta\tau_{Refl} = \tau_{Refl} - \tau_0$ are the code phase errors of the LOS and reflected signal in chips, respectively. T is the coherent integration time, and it should be set to an appropriate value so that the integrate and dump process does not cross the navigation data bit transition boundaries. Therefore, the navigation data bit value $D(n)$ can be assumed to be a constant.

In the digital phase tracking loop, the I- and Q-channel output can be characterized by the relative phase and amplitude. To avoid possible confusion, this paper describes the difference between the incoming signal and receiver local replica signal parameters as the 'error'; the difference between the incoming LOS signal and reflected signal parameters as the 'shift'; and the difference between receiver measurement and LOS signal parameters as the 'measurement error'. For example,

$f_{LOS,n} - \tilde{f}^{-}_{0,n}$ = Frequency error of LOS signal

$f_{Refl,n} - \tilde{f}^{-}_{0,n}$ = Frequency error of reflected signal

$f_{Refl,n} - f_{LOS,n}$ = Frequency shift of reflected signal

$\tilde{f}_{0,n} - f_{LOS,n}$ = Receiver Doppler measurement error

$f_{LOS,n}$, $f_{Refl,n}$ and $\tilde{f}^{-}_{0,n}$ are the Doppler frequencies of the LOS signal, reflected signal, and receiver-predicted Doppler frequency at epoch n, respectively. The symbol $(\sim)$ indicates the receiver's local replica value, and $(-)$ is the predicted value. $A_{LOS,n}$ denotes the amplitude of the LOS signal at epoch n, which can be expressed as a function of the frequency error

$$\begin{aligned} A_{LOS,n} &= \frac{N\sqrt{C_{LOS,n}}R(\Delta\tau_{LOS,n})}{\frac{1}{2}\left(\omega_{LOS,n}-\omega_{0,n}\right)T}\sin\left(\left(\omega_{LOS,n}-\omega_{0,n}\right)\frac{T}{2}\right) \\ &= N\sqrt{C_{LOS,n}}R(\Delta\tau_{LOS,n})\mathrm{sinc}\left(\left(f_{LOS,n}-\tilde{f}^{-}_{0,n}\right)T\right) \end{aligned} \tag{9}$$

where N is the number of sample values in the integration time. Similarly, the amplitude of the reflected signal component at epoch n is

$$A_{Refl,n} = N\sqrt{C_{Refl,n}}R(\Delta\tau_{Refl,n})\mathrm{sinc}\left(\left(f_{Refl,n}-\tilde{f}^{-}_{0,n}\right)T\right) \tag{10}$$

The carrier phase error of the LOS and reflected signal components can also be written as

$$\phi_{LOS,n} = 2\pi\left(f_{LOS,n}-\tilde{f}^{-}_{0,n}\right)\left(t_0+\frac{T}{2}\right)+\vartheta_{LOS,n}-\vartheta_{0,n} \tag{11}$$

$$\phi_{Refl,n} = 2\pi\left(f_{Refl,n}-\tilde{f}^{-}_{0,n}\right)\left(t_0+\frac{T}{2}\right)+\vartheta_{Refl,n}-\vartheta_{0,n} \tag{12}$$

Therefore, the phase error for every epoch consists of the average phase error due to the frequency error and the initial phase error. Finally, the correlation output can be simplified

$$I_p(n) = A_{LOS,n}\cos\phi_{LOS,n} + A_{Refl,n}\cos\phi_{Refl,n} \tag{13}$$

$$Q_p(n) = A_{LOS,n}\sin\phi_{LOS,n} + A_{Refl,n}\sin\phi_{Refl,n} \tag{14}$$

The carrier synchronization is usually achieved by a carrier phase tracking loop, which is often implemented as a phase-locked loop (PLL). The PLL discriminator estimates the signal carrier phase error between the incoming and local replica signals. The additional energy of the reflected signal with different relative phases causes the compound signal to be tracked instead. The carrier phase error of the compound signal at epoch n can be expressed as

$$\phi_{MP,n} = \arctan(Q_p(n)/I_p(n)) \tag{15}$$

$\arctan$ is the two-quadrant arctangent function.

However, tracking the carrier phase directly in some real applications can be challenging since it is susceptible to user dynamics. In order to help with phase monitoring with dynamic robustness and to increase efficiency, many receivers employ frequency tracking [26]. The type of discriminator determines whether this is a PLL or a FLL. The frequency discriminator measures the frequency/Doppler frequency difference between the incoming signal and the local carrier [1]. The Doppler frequency error $\delta f_{0,n}$ is equivalent to the change of the carrier phase error between two adjacent epochs, which can be obtained as

$$\delta f_{0,n} = \frac{\phi_{MP,n} - \phi_{MP,n-1}}{2\pi T} \tag{16}$$

The change of the carrier phase error between two epochs can be monitored with the two-quadrant arctangent or the four-quadrant arctangent ($\arctan 2$) functions. For example, the change in the carrier phase error can be written as (17) where P_{cross} and P_{dot} are calculated based on trigonometric manipulations

$$P_{dot} = I_p(n)I_p(n-1) + Q_p(n)Q_p(n-1) \tag{18}$$

$$P_{cross} = Q_p(n)I_p(n-1) - I_p(n)Q_p(n-1) \tag{19}$$

The detailed calculation is displayed in Appendix A. Similar models can be derived for the $\arctan 2$-based frequency discriminator. It is worth noting that the principal value of the carrier phase error change lies between $-\pi$ and π when applying the $\arctan 2$ function. Therefore, with the knowledge of the carrier phase error and amplitude of the LOS and reflected signal components, the prompt correlator output and the frequency discriminator output can be estimated.

Fig. 2. presents a vector diagram that includes the LOS signal, the reflected signal, and the compound signal components. This diagram demonstrates an example where the carrier phase error of the LOS signal remains unchanged in adjacent epochs. It is used to illustrate the relationships among the signal components and visualize the Doppler multipath error. The area shaded in blue is the change in the carrier phase error due to the multipath effect, which is equivalent to the Doppler multipath error.

The FLL is a feedback control loop comprising the correlator, a discriminator, a loop filter, and a carrier generator. The discriminator's output is the input of the loop filter. Diverse loop filters, distinguished by their

$$
\begin{aligned}
I_p(n) &= \frac{1}{T}\int_{t_0}^{t_0+T} i_p(t)dt \\
&\approx \frac{1}{T}\int_{t_0}^{t_0+T} \left(\sqrt{C_{LOS}}D(t-\tau_{LOS})x(t-\tau_{LOS})x(t-\tau_0)\cos\left(\left(\omega_{LOS}-\omega_0\right)t+\vartheta_{LOS}-\vartheta_0\right)\right)dt \\
&+ \frac{1}{T}\int_{t_0}^{t_0+T} \left(\sqrt{C_{Refl}}D(t-\tau_{Refl})x(t-\tau_{Refl})x(t-\tau_0)\cos\left(\left(\omega_{Refl}-\omega_0\right)t+\vartheta_{Refl}-\vartheta_0\right)\right)dt \\
&= \frac{\sqrt{C_{LOS}}D(n)R(\Delta\tau_{LOS})}{\frac{1}{2}\left(\omega_{LOS}-\omega_0\right)T}\sin\left(\left(\omega_{LOS}-\omega_0\right)\frac{T}{2}\right)\cos\left[\left(\omega_{LOS}-\omega_0\right)\left(t_0+\frac{T}{2}\right)+\vartheta_{LOS}-\vartheta_0\right] \\
&+ \frac{\sqrt{C_{Refll}}D(n)R(\Delta\tau_{Refll})}{\frac{1}{2}\left(\omega_{Refl}-\omega_0\right)T}\sin\left(\left(\omega_{Refl}-\omega_0\right)\frac{T}{2}\right)\cos\left[\left(\omega_{Refl}-\omega_0\right)\left(t_0+\frac{T}{2}\right)+\vartheta_{Refl}-\vartheta_0\right]
\end{aligned} \tag{7}
$$

$$
\begin{aligned}
Q_p(n) &= \frac{1}{T}\int_{t_0}^{t_0+T} q_p(t)dt \\
&\approx \frac{\sqrt{C_{LOS}}D(n)R(\Delta\tau_{LOS})}{\frac{1}{2}\left(\omega_{LOS}-\omega_0\right)T}\sin\left(\left(\omega_{LOS}-\omega_0\right)\frac{T}{2}\right)\sin\left[\left(\omega_{LOS}-\omega_0\right)\left(t_0+\frac{T}{2}\right)+\vartheta_{LOS}-\vartheta_0\right] \\
&+ \frac{\sqrt{C_{Refl}}D(n)R(\Delta\tau_{Refl})}{\frac{1}{2}\left(\omega_{Refl}-\omega_0\right)T}\sin\left(\left(\omega_{Refl}-\omega_0\right)\frac{T}{2}\right)\sin\left[\left(\omega_{Refl}-\omega_0\right)\left(t_0+\frac{T}{2}\right)+\vartheta_{Refl}-\vartheta_0\right]
\end{aligned} \tag{8}
$$

$$
\begin{aligned}
&\phi_{MP,n}-\phi_{MP,n-1} = \arctan\left(\frac{P_{cross}}{P_{dot}}\right) \\
&= \arctan\left(\frac{\begin{array}{l}A_{LOS,n}A_{LOS,n-1}\sin(\phi_{LOS,n}-\phi_{LOS,n-1})+A_{LOS,n}A_{Refl,n-1}\sin(\phi_{LOS,n}-\phi_{Refl,n-1}) \\ +A_{Refl,n}A_{LOS,n-1}\sin(\phi_{Refl,n}-\phi_{LOS,n-1})+A_{Refl,n}A_{Refl,n-1}\sin(\phi_{Refl,n}-\phi_{Refl,n-1})\end{array}}{\begin{array}{l}A_{LOS,n}A_{LOS,n-1}\cos(\phi_{LOS,n}-\phi_{LOS,n-1})+A_{LOS,n}A_{Refl,n-1}\cos(\phi_{LOS,n}-\phi_{Refl,n-1}) \\ +A_{Refl,n}A_{LOS,n-1}\cos(\phi_{Refl,n}-\phi_{LOS,n-1})+A_{Refl,n}A_{Refl,n-1}\cos(\phi_{Refl,n}-\phi_{Refl,n-1})\end{array}}\right)
\end{aligned} \tag{17}
$$

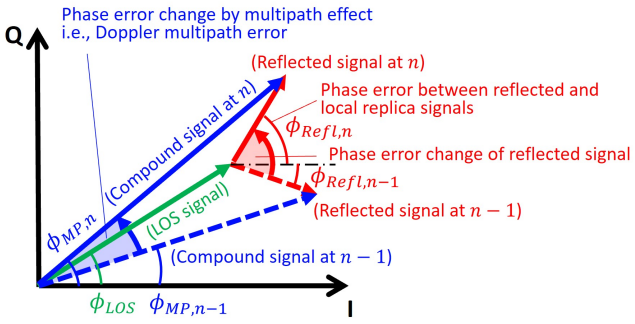

Fig. 2. A vector diagram of phase error shift with one reflected signal component.

designs and parameter settings, exhibit varying loop stability and tracking performance [1]. For instance, traditional scalar tracking loops usually employ second-order or higher-order loop filter designs for tracking a single channel, whereas vector tracking-based receivers, relying on navigation filters, estimate signal parameters by integrating tracking information from multiple channels [27, 28, 29]. In practical receiver setups, these filters are designed for the purpose of enhancing noise management and dynamic tracking capabilities [30, 23]. In sum, the discriminator output serves as the measurement residual for the prediction of the measurement and provides the update for the next epoch's correlation and integration.

This study aims to illustrate the typical performance of FLL under multipath interference without averaging sample values during navigation processing. Therefore, the measurement update interval corresponds to the coherent integration time. The loop filter produces the estimated Doppler error indicated as $\delta\hat{f}_{0,n}$. Ultimately, the estimated Doppler error is updated, and the receiver Doppler measurement is obtained

$$
\tilde{f}_{0,n} = \tilde{f}_{0,n-1} + \delta\hat{f}_{0,n} \tag{20}
$$

The receiver-predicted Doppler frequency at the next epoch is updated

$$
\tilde{f}^{-}_{0,n+1} = \tilde{f}_{0,n} \tag{21}
$$

In sum, in FLL, the receiver estimates the Doppler frequency by monitoring the Doppler frequency error of the compound signal over the continuous tracking time. Therefore, the Doppler frequency of the compound signal biases the receiver replica signal and causes an error in the receiver Doppler measurement. The receiver Doppler measurement error, or equivalently, the Doppler multipath error, is defined as the difference between the Doppler frequency of the LOS signal and the receiver-measured Doppler frequency as

$$
f_{error,n} = \tilde{f}_{0,n} - f_{LOS,n} \tag{22}
$$

In conclusion, the receiver Doppler multipath error is time-varying based on the amplitude and carrier phase error of the LOS and reflected signals in the continuous tracking time. It's worth mentioning that the carrier phase errors of the signal components represent the total phase difference between the incoming signal and the receiver replica, including the frequency error part and the initial carrier phase error part. The initial carrier phase error is time-varying due to environmental influences on the incoming signal and may also change due to the receiver's local replica's carrier phase updates. Therefore, in the FLL-only architecture, only the frequency error can be estimated. In other words, the ambiguity of carrier phase error exists. Without further knowledge of the PLL, the signal vectors move along a circle with a radius of signal amplitude and can point in any direction.

A. Pseudorange rate error envelope

The pseudorange rate error due to multipath interference can be expressed as

$$\dot{\rho}_{error,n} = \lambda f_{error,n} \tag{23}$$

The theoretical deviations in the previous sections indicate that the frequency discriminator output is predominantly influenced by the signal parameters at the adjacent epochs. Several assumptions are made to streamline the analysis process in this section. First, it is assumed that there is no receiver update between the two epochs, such that $\tilde{f}^{-}_{0,n-1} = \tilde{f}^{-}_{0,n}$ and $\vartheta_{0,n-1} = \vartheta_{0,n}$. Second, the receiver accurately tracks the LOS signal at the preceding epoch $n-1$ and the LOS signal carrier phase remains constant, such that $\phi_{LOS,n} - \phi_{LOS,n-1} = 0$. Third, it is assumed that the reflected signal injects at epoch n, then $A_{Refl,n-1} = 0$. Therefore, the frequency and phase errors of the reflected signal can be expressed as the frequency and phase shifts of the reflected signal with respect to the LOS signal, denoted as $f_{shift,n}$ and $\vartheta_{shift,n}$. According to (16), (17) and (23), the multipath pseudorange rate error can be simplified as (24). The amplitude of the signal components at the two epochs are similar and can be derived from (9) and (10) as

$$A_{LOS,n} = N\sqrt{C_{LOS,n}}R(\Delta\tau_{LOS,n}) \tag{25}$$

$$A_{Refl,n} = N\sqrt{C_{Refl,n}}R(\Delta\tau_{Refl,n})\mathrm{sinc}(f_{shift,n}T) \tag{26}$$

The mathematical models can be used to visualize the Doppler multipath and pseudorange rate errors induced by the reflected signal in the specific scenario. For example, Fig. 3 (a) plots the pseudorange rate error and Doppler multipath error envelopes for a binary phase shift keying (BPSK) signal under different coherent integration times and received reflected signal-to-direct signal (R/D) power ratios. The x-axis values are normalized by the coherent integration time. A normalized frequency shift value of 1 corresponds to the FLL discriminator pull-in range of $1/T$. In this plot, the influence of the carrier phase shift of the reflected signal is neglected ($\vartheta_{shift,n} = 0$). When T and R/D power ratio remain unchanged, the upper bound of the pseudorange rate error occurs when the amplitude of the reflected signal vector is large, such as when the code phase errors of the LOS and reflected signals have the same magnitude ($R(\Delta\tau_{Refl,n}) = R(\Delta\tau_{LOS,n})$). The shaded areas with the same colors indicate cases where $R(\Delta\tau_{Refl,n}) < R(\Delta\tau_{LOS,n})$. This occurs because larger code phase errors result in smaller values in the ACF, thereby decreasing the amplitude of the signal vector. The envelopes cross zero when the normalized frequency shift is 0.5, due to the zero value of $\sin(2\pi f_{shift,n}T + \vartheta_{shift,n})$ in (24). As the $f_{shift,n}$ increases, the pseudorange rate error becomes negative due to the properties of trigonometric functions. Additionally, a lower bound of the pseudorange rate error is observed with increasing $f_{shift,n}$. This occurs because the amplitude of the reflected signal vector degrades according to $\mathrm{sinc}\,(f_{shift,n}T)$ in (26). In summary, the pseudorange rate error decreases with longer coherent integration times and a lower reflected signal amplitude. Fig. 3 (b) illustrates the pseudorange rate and Doppler multipath errors across different carrier phase shifts of the reflected signal. In this plot, the pseudorange rate error varies significantly with different settings of $\vartheta_{shift,n}$. The maximum (max) and minimum (min) error bounds are identified, showing decreasing errors as $f_{shift,n}$ increases. The possible reason is the attenuation of the reflected signal amplitude caused by a larger $f_{shift,n}$. A detailed derivation of the maximum and minimum error bounds is provided in Appendix B.

BPSK modulation is regarded as the most basic spreading modulation for satellite navigation, whereas binary offset carrier (BOC) modulation is a more complex technique that employs subcarriers. In (25) and (26), the normalized ACF with respect to a code phase shift τ for the BPSK and sine-phase BOC signals can be expressed as [31]

$$R(\tau) = \begin{cases} \Lambda_{BPSK}(\tau), \text{ for BPSK} \\ \Lambda_{BOC}(\tau) + \sum_{k=1}^{M-1}(-1)^k(1-\frac{k}{M})\Lambda_{BOC}\left(|\tau| - kT_{sub}\right), \text{ for BOC} \end{cases} \tag{27}$$

where

$$\Lambda_{type}(\tau) \triangleq \begin{cases} 1 - \frac{|\tau|}{T_{type}} & , |\tau| \le T_{type} \\ 0 & , \text{ otherwise} \end{cases} \tag{28}$$

T_{type} = chip width of the PRN code, for BPSK signal

T_{type} = chip width of the subcarrier, for BOC signal

For a specific BOC modulation denoted as BOC(j,k), $M = 2j/k$ represents the order of the BOC modulation, and T_{sub} is the chip width of the subcarrier. Assume that the code phase error of the LOS signal is zero, such that $\Delta\tau_{LOS,n} = 0$ and $\Delta\tau_{Refl,n} = \tau_{shift,n}$. The code phase shift of the reflected signal, $\tau_{shift,n}$, represents the code phase difference between the LOS and reflected signals. According to (24), the comparison between the BOC(1,1) signal and the BPSK signal is plotted in Fig.

$$\dot{\rho}_{error,n} = \frac{\lambda}{2\pi T} \arctan\left(\frac{A_{Refl,n} A_{LOS,n-1} \sin(2\pi f_{shift,n} T + \vartheta_{shift,n})}{A_{LOS,n} A_{LOS,n-1} + A_{Refl,n} A_{LOS,n-1} \cos(2\pi f_{shift,n} T + \vartheta_{shift,n})} \right) \tag{24}$$

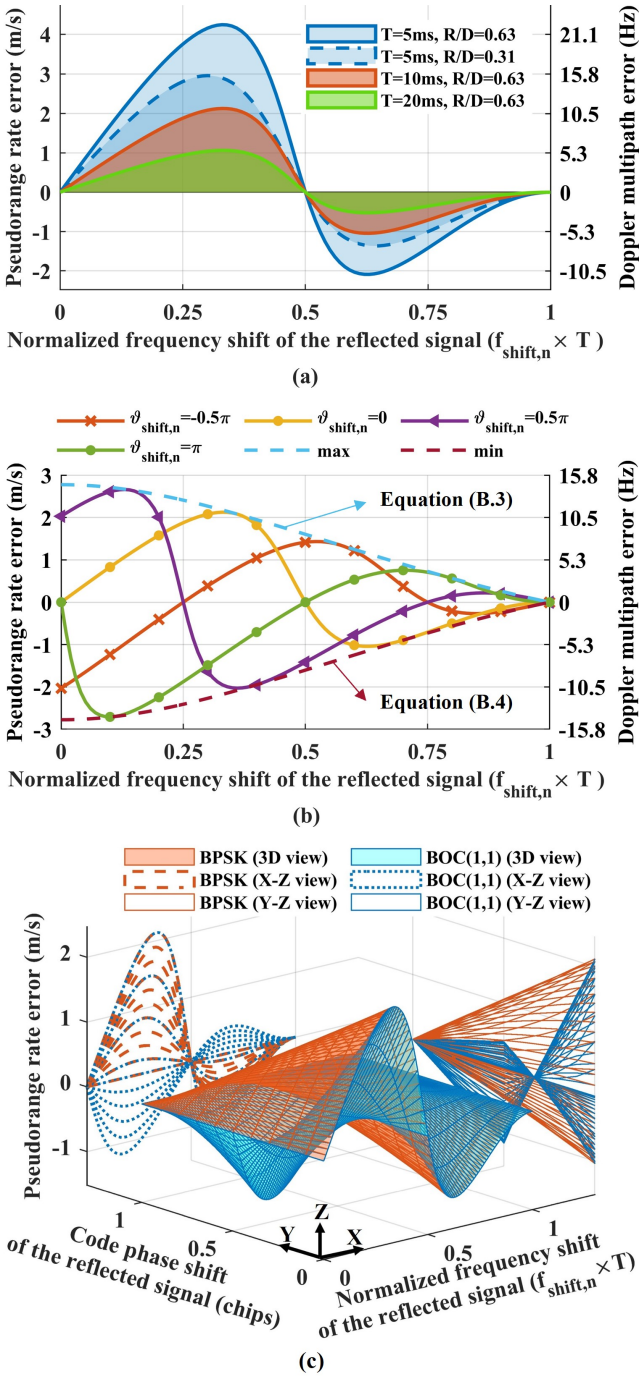

Fig. 3. (a) Example of Doppler multipath error and pseudorange rate error envelopes versus reflected signal frequency shift for a BPSK signal when $\vartheta_{shift,n} = 0$, under varying coherent integration times T and R/D power ratios. (b) Example of Doppler multipath error and pseudorange rate error envelopes for a BPSK signal when $T = 10$ milliseconds (ms) and $R/D = 0.63$, under varying $\vartheta_{shift,n}$. (c) Example of pseudorange rate error envelopes for BOC(1,1) and BPSK signals, when $\vartheta_{shift,n} = 0$, T = 10ms and R/D = 0.63, under varying $f_{shift,n}$ and $\tau_{shift,n}$.

3 (c). The projection of the pseudorange rate error in both the frequency shift and code phase shift domains is presented. The X-Z view illustrates the pseudorange rate error with respect to the $f_{shift,n}$, which mirrors Fig. 3 (a) for the BPSK signal. For the BOC signal, the pseudorange rate error spans a wider range due to the negative side peak in the ACF of the BOC(1,1) signal [31]. In terms of absolute pseudorange rate error envelopes, both BPSK- and BOC-modulated signals exhibit similar behavior. The Y-Z view shows the pseudorange rate error decreases as $\tau_{shift,n}$ increases. This is because the reflected signal's amplitude in the prompt correlator degrades significantly with increasing $\tau_{shift,n}$. For the BOC signal, the pseudorange rate error decreases more rapidly than for the BPSK signal, with a zero-crossing point due to the properties of the BOC(1,1) ACF. In conclusion, regarding absolute pseudorange rate error, multipath interference has a smaller impact on BOC-modulated signals because of the nature of the BOC correlation curve.

There are two noteworthy points about the introduced error envelopes. First, this model only describes limited multipath scenarios in a noise-free environment ($\delta\hat{f}_{0,n} = \delta f_{0,n}$). Second, the presented envelopes depict the instantaneous Doppler measurement error, whereas the Doppler measurement error undergoes dynamic variations within the continuous feedback tracking loop. Despite the non-realistic nature of this model, it demonstrates a quick characterization of the receiver measurement behavior in specific scenarios.

IV. A RAY-TRACING-AIDED FLL SIMULATOR

This section introduces an FLL simulator to visualize the practical performance of the receiver frequency tracking process in urban environments. In Section IV. A, the Doppler frequency models are introduced to eliminate errors due to the receiver clock bias. In order to mitigate the impact of thermal noise, the noise-induced error is simulated based on predicting the receiver tracking loop parameters, which will be covered in more detail in Section IV. B. The simulated receiver-measured Doppler frequency is compared with the Doppler measurements collected from the commercial GNSS receiver at the same experimental locations for validation purposes in Section V. The overall structure of the proposed FLL simulator and performance validation process are depicted in Fig. 4, where x and x^s are the user and satellite positions, respectively.

The proposed FLL simulator comprises two main components: the receiver frequency tracking loop and the ray-tracing algorithm. The ray-tracing algorithm developed in [32] estimates the optical satellite-reflector-user

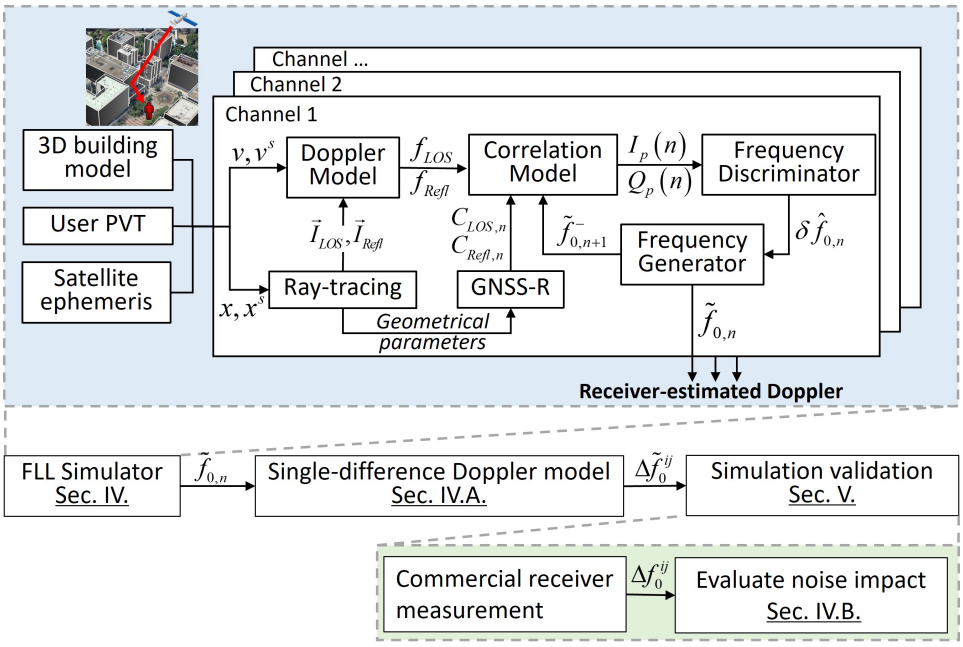

Fig. 4. The flowchart of the proposed ray-tracing-aided FLL simulator and validation processes.

geometry in the urban environment, utilizing the satellite ephemeris, the 3D building model, and the user PVT information. The reception of signals can be categorized into three types based on the number of simulated signal paths: the LOS case, which involves only a direct signal; the non-line-of-sight case, which involves a reflected signal; and the multipath case, which receives direct and reflected signals simultaneously. The attenuation of the reflected signal power depends on the properties of the reflector surface materials [24]. Thus, the ray-tracing algorithm assumes a smooth building surface and considers the signal reflection to be specular. In this algorithm, the GNSS-reflectometry (GNSS-R) model is employed to estimate the carrier-to-noise ratio (C/N_0) of the reflected signal. This estimation depends on factors including C/N_0 in the open-sky model, reflection coefficient, and signal propagation path [32]. Algorithm 1 outlines the processes involved in the ray-tracing algorithm.

Subsequently, the Doppler frequency values of the LOS and reflected signals are supplied to the correlation model for calculation of the I- and Q-channel output. The interval for generating the correlation output depends on the coherent integration time, which is restricted to a maximum of 20ms. The correlation output and receiver-measured Doppler frequency are updated at every epoch to simulate receiver continuous tracking. In addition, simulations are first conducted in a noise-free environment, and the tracking loop errors are subsequently analyzed utilizing loop filter parameters outlined in Section IV. B. The receiver-measured Doppler frequency is then computed by accumulating the tracked Doppler error. Algorithm 2 outlines the key steps of the simulation. The fifth step of this algorithm involves adjusting the simulator's output frequency to a standard commercial receiver output frequency, such as 1Hz, for simulation validation. In this work, the dynamic code tracking performance is not considered, and the code tracking error is set to zero in the small delay multipath scenario.

Algorithm 1 Ray-tracing algorithm [32]

Input: User receiver PVT, satellite position, 3D building model

Output: $\vec{I}_{LOS}$, $\vec{I}_{Refl}$, $C_{LOS,n}$, $C_{Refl,n}$, f_{LOS}, f_{Refl}

1: **Search possible signal propagation path:** It is assumed that the signal propagation path is a straight line. Only the signal without any intersection with the 3D building model surfaces will be considered as LOS type. Define $\vec{I}_{LOS}$ and $\vec{I}_{Refl}$.

2: **Signal strength estimation:** The reflected signal power is $C/N_{0,Refl} = C/N_{0,LOS} + 20\log\left(\frac{s_{LOS}}{s_{Refl1}+s_{Refl1}}|\kappa_r|\right)$, where $C/N_{0,LOS}$ is the LOS signal power estimated based on the satellite elevation-C/N_0 relationship. s_{LOS} is the distance between the satellite and receiver. s_{Refl1} and s_{Refl2} are the distance between the satellite and reflection point and the distance between the reflection point and receiver, respectively. κ_r is a predefined reflection coefficient.

3: **Doppler of the received signal:** Compute f_{LOS} and f_{Refl} based on (1) and (4).

According to (17), the evaluation of the receiver-measured Doppler frequency necessitates knowledge of each signal component's amplitude and carrier phase error. The signal vector amplitude depends on the C/N_0 and frequency difference between the incoming signal and the replica signal, which can be estimated based on the signal strength provided by the ray-tracing result and the receiver frequency tracking results. However, the

Algorithm 2 Receiver frequency tracking

Input: Ray-tracing results

Output: $\tilde{f}_{0,n}$, $f_{error,n}$

1: **Classify satellite type:** Select the satellites with more than two possible propagation paths.
2: **Amplitude of signal components:** Compute $A_{type,n}$ based on (9) and (10), where $C_{type,n}$ and $f_{type,n}$ are given by Algorithm 1. T is predefined according to Algorithm 3. $\Delta\tau_{type}$ is set to zero to neglect the code tracking error.
3: **Carrier phase error of signal components:** Compute $\phi_{type,n}$ based on (11) and (12). $\vartheta_{Refl,n} - \vartheta_{0,n}$ is neglected due to the unknown cycle of ambiguity and PLL architecture.
4: **Frequency tracking:** Calculate correlation results and discriminator output. $\tilde{f}_{0,n}$ is updated in each epoch.
5: **Output frequency adjustment:** Simulator output $\tilde{f}_{0,m} \in \left[\tilde{f}_{0,n}, \tilde{f}_{0,n+M}\right]$, where m is based on the desired output rate and M is determined by T.
6: **Receiver velocity estimation:** The least-squares (LS) method is applied to simulate the receiver velocity based on the $\tilde{f}_{0,m}$ of visible satellites.

carrier phase error encapsulates the total phase difference, including the initial carrier phase error and the frequency difference between the incoming signal and the replica signal. Simulating the initial carrier phase error of each signal component presents a significant challenge due to several factors. First, the carrier phase is sensitive to user dynamics and the potential variety of interference in the real environment. Second, the ray-tracing technique currently lacks the capability to predict the signal rays and reflection points with centimeter-level accuracy. Furthermore, the receiver carrier phase update process and the integer number of cycles are unpredictable due to the unknown tracking loop architecture and oscillator of the commercial receiver [23]. Therefore, achieving point-to-point simulation is difficult. The proposed simulator is thus designed to estimate the possible distribution and evolution pattern of the receiver-measured Doppler frequency.

A. Single-difference Doppler measurement model

The proposed simulator operates in a noise-free environment, whereas real Doppler measurements are susceptible to various interferences. A single-difference Doppler frequency model is introduced to eliminate extraneous interference during real experiments. In the GNSS receiver, the Doppler frequency, or equivalently the pseudorange rate, is utilized for receiver velocity estimation and may be biased, which can be modeled as [25]

$$\lambda\tilde{f}_0^i = \lambda f_{LOS}^i + \dot{b}_u + \dot{b}^i - \dot{I}^i + \dot{T}^i + \lambda\varepsilon_{FLL}^i + \lambda f_{error}^i \tag{29}$$

where $\tilde{f}_0^i$ is the receiver-measured Doppler frequency of a test satellite i. $\lambda f_{LOS}^i = \left(v - v^i\right) \cdot \vec{I}_{LOS}^i$ is the received LOS signal Doppler frequency due to relative motion between the user and satellite. $\dot{b}_u$ and $\dot{b}^i$ are the rates of change in the receiver and satellite clocks (m/s), respectively. $\dot{I}^i$ and $\dot{T}^i$ are the changes in error due to ionosphere and troposphere interference, respectively. f_{error}^i is the Doppler multipath error. ε_{FLL}^i denotes the error in the FLL. It is modeled here to consist of two dominant sources of error: the thermal noise σ_{tFLL}^i and the dynamic stress f_e. Therefore, the standard deviation of the FLL error is $std\left\{\varepsilon_{FLL}^i\right\} = \sigma_{tFLL}^i + \frac{f_e}{3}$. The 1-sigma frequency jitter caused by thermal noise is [1]

$$\begin{aligned}\sigma_{tFLL} &= \frac{1}{2\pi T}\sqrt{\frac{4FB_n}{C/N_0}\left(1 + \frac{1}{TC/N_0}\right)} \\ F &= 1 \text{ for high } C/N_0 \\ &= 2 \text{ for low } C/N_0 \text{ near threshold} \\ B_n &= \text{Noise Bandwidth (Hz)}\end{aligned} \tag{30}$$

The dynamic stress error is calculated based on the steady-state error in the FLL, which is determined by a given user-satellite dynamic and the tracking loop architecture. Therefore, the dynamic stress error for different loop filter architectures varies. To simplify our analysis, it is assumed that a high-order FLL is utilized to precisely track the carrier frequency, and the dynamic stress error is small. In addition, the changes in ionospheric delay, troposphere delay, and satellite clock error are relatively small over a short period of time and can be ignored. Then, (29) can be simplified as

$$\lambda\tilde{f}_0^i = \lambda f_{LOS}^i + \dot{b}_u + \lambda\varepsilon_{tFLL}^i + \lambda f_{error}^i \tag{31}$$

where ε_{tFLL}^i is the thermal noise error. The single-difference Doppler frequency (SDD) is defined as the Doppler difference between a test satellite i, and a reference satellite j consisting of a LOS signal only. It can be written as

$$f_{type}^{ij} = f_{type}^i - f_{LOS}^j \tag{32}$$

where f_{type}^i and f_{LOS}^j are the Doppler frequencies from the same test. The user clock error is the same for all satellites in the same test, and its impact can be removed by calculating the SDD. Therefore, SDD of the receiver Doppler measurement $\tilde{f}_0^{ij}$ is

$$\tilde{f}_0^{ij} = f_{LOS}^{ij} + \varepsilon_{tFLL}^{ij} + f_{error}^i \tag{33}$$

Assume that there is no correlation between the noise of the two satellites. Therefore, the variance of thermal noise contained in satellites i and j is

$$\text{var}\left\{\varepsilon_{tFLL}^{ij}\right\} = \left(\sigma_{tFLL}^{ij}\right)^2 = \left(\sigma_{tFLL}^i\right)^2 + \left(\sigma_{tFLL}^j\right)^2 \tag{34}$$

Define the single-difference Doppler error (SDDE) as $\Delta\tilde{f}_0^{ij} = \tilde{f}_0^{ij} - f_{LOS}^{ij}$. Therefore, $\Delta\tilde{f}_0^{ij}$ consists of thermal noise only if satellite i is LOS, and additional error by

multipath is involved if satellite i is multipath type. $\Delta\tilde{f}_0^{ij}$ can be fit into a Gaussian distribution model expressed as

$$\Delta\tilde{f}_0^{ij} \begin{cases} \sim N\left(0, \text{var}\left(\varepsilon_{tFLL}^{ij}\right)\right), i \text{ is LOS} \\ \sim N\left(f_{error}^{i}, \text{var}\left(\varepsilon_{tFLL}^{ij}\right)\right), i \text{ is MP} \end{cases} \tag{35}$$

Therefore, the variance of the SDDE is mainly dominated by thermal noise, and the change in the mean value of the SDDE can be used to identify the test satellite's signal reception type.

B. Examination of noise impact

According to Section IV. A, the variance of SDDE is dominated by thermal noise. Therefore, the impact of thermal noise needs to be appropriately estimated for the proposed simulator validation. The receiver tracking loop parameters, including the noise bandwidth and coherent integration time, significantly influence the thermal noise error. Sometimes, it is difficult to discern these parameters from commercial receivers. The 68–95–99 rule is used to predict the receiver tracking loop parameter and enhance the reliability of the simulation validation process. The well-known 68–95–99 rule, also called the empirical rule, predicts that in normal distributions, 68% of the data falls within one standard deviation (1-sigma), 95% percent within two standard deviations (2-sigma), and 99.7% within three standard deviations (3-sigma). Therefore, if the test satellite is of the LOS type, the SDDE value should comply with this rule. The primary procedures for predicting the real receiver tracking loop parameters and evaluating the thermal noise impact are summarized in Algorithm 3.

Algorithm 3 Receiver tracking loop parameter estimation based on thermal noise error

Input: Doppler measurement from a real receiver and ray-tracing results

Output: B_n and T

1: **Choose LOS satellites:** Based on ray-tracing results, select the test and reference satellites, which are all classified as LOS.
2: **Calculate SDDE of real measurement:** Calculate $\Delta f_0^{ij} = f_0^{ij} - f_{LOS}^{ij}$, where f_0^{ij} is the SDD from the real receiver. f_{LOS}^{ij} is the simulated SDD of the LOS signal.
3: **Set possible B_n and T:** Calculate σ_{tFLL}^{ij} based on (30) and (34). The C/N_0 is obtained from the real receiver measurement.
4: **Test if Δf_0^{ij} satisfies the 68-95-99 rule:** Set the different values of B_n and T, and repeat from step one until Δf_0^{ij} satisfy the theoretical two standard deviation distribution.
5: **Test MP satellites:** If the test satellite is multipath type, Δf_0^{ij} should not satisfy the theoretical distribution with zero mean and σ_{tFLL}^{ij}.

V. EXPERIMENT

A. Experimental setup

The experimental equipment is depicted in Fig. 5. The 3D Light Detection and Ranging (LiDAR) sensor HDL 32E Velodyne provides a relatively high-precision ground truth with an inaccuracy of around 0.3 meters [33]. The common commercial-grade GNSS receiver, u-blox EVK-F9P, is utilized to provide the real Doppler measurements for the simulator performance validation. Experiments were conducted in suburban areas in Tsim Sha Tsui, Hong Kong, on July 15, 2023. Fig. 6. illustrates two data collection scenarios in Google Earth with trajectory denoted by the red arrows and the receiver velocity in the East-North-Up (ENU) frame. The experiments are located in areas near a tall building with flat walls on one side and an open sea on the other side. This setting enables LOS signals from the open sky to remain unobstructed. The 3D LiDAR sensor and the u-blox receiver were affixed to the same trolley, which was carried by a pedestrian moving reciprocally along the trajectories approximately perpendicular to the building surfaces. This specific configuration aims to maximize the frequency shift of the reflected signal [34]. The duration of data collection for scenario 1 (S1) spanned approximately 85 seconds, and it was around 56 seconds for scenario 2 (S2). The subfigures on the right side of Fig. 6. are sky-plots with building boundaries in gray areas and display the visible Global Positioning System (GPS) L1 satellites. Satellites depicted in green are categorized as the LOS type, while those in yellow signify the multipath (MP) type based on ray-tracing results. No alterations in the satellite type occurred during the tests. Table I summarizes the parameter settings for the proposed simulator.

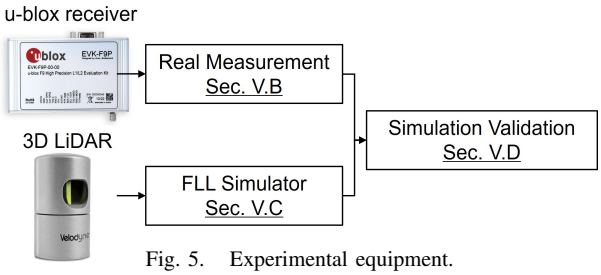

Fig. 5. Experimental equipment.

TABLE I
Parameter settings of the simulation

Frequency discriminator	$\arctan 2$
Coherent integration time (T)	10ms
Noise bandwidth (B_n)	15Hz
Reflection coefficient (κ_r)	0.6
Reference satellites	S1-PRN 5, S2-PRN 5

B. Analysis of the real Doppler measurement

In this section, Doppler measurements obtained from the commercial receiver are analyzed. The proposed

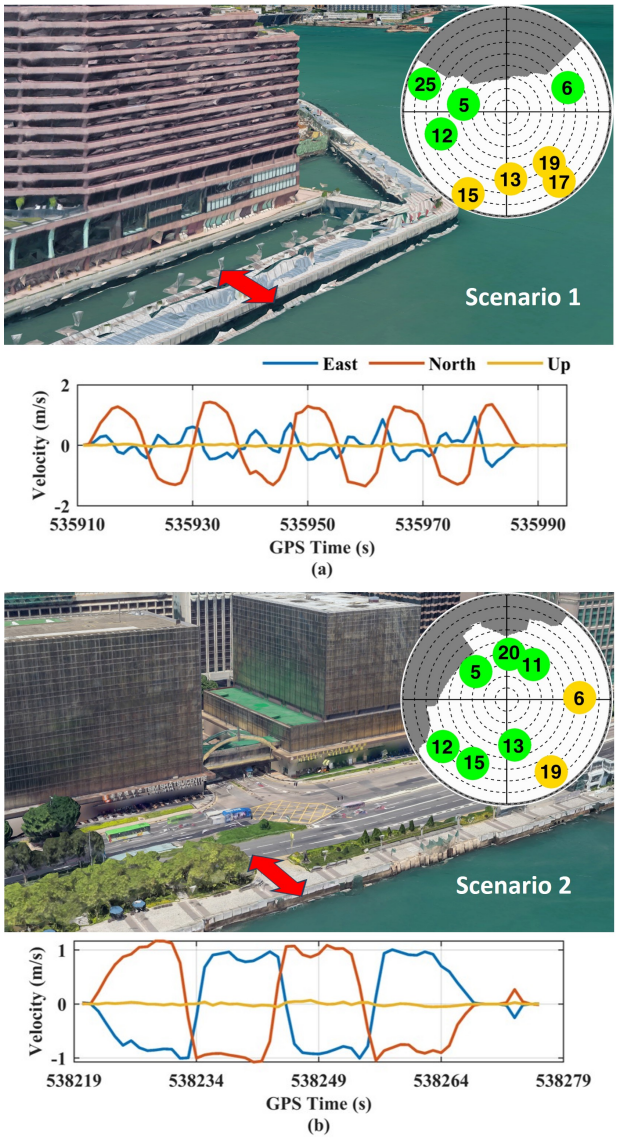

Fig. 6. Data collection location, sky-plots with visible satellites, and ground truth velocity in (a) scenario 1 and (b) scenario 2. Green PRN for LOS type, yellow for MP type.

SDDE model in (35) is utilized to discuss the influence of the reflected signal and thermal noise in real measurements. Fig. 7. displays the SDDE values of the visible test satellites. The results depicted in blue correspond to the LOS satellites, while the plots in orange represent satellites classified as multipath. The results exhibit fluctuations centered around zero, with the multipath satellites displaying larger fluctuations compared to the LOS satellites. Table II quantitatively summarizes the standard deviation (STD) of the test satellites. In scenario 1, the LOS satellites exhibit STDs of no more than 3Hz, whereas the majority of multipath satellites demonstrate STDs exceeding 3Hz. Notably, PRN 13 displays an STD of about 2.6Hz, which is similar to that of the LOS PRN 6. There are two possible reasons: either PRN 13 is incorrectly categorized as multipath while it is, in fact, the LOS type, or the influence from the reflected signal in the Doppler measurements of PRN 13 is small. For scenario 2, the STDs of LOS satellites range from 1 to 3.5Hz, while multipath satellites show STDs surpassing 4.3Hz. Recall that SDDE consists of only noise when the test satellite is LOS, while the error from the reflected signal is added when the test satellite is multipath. Therefore, the amplified oscillation observed in the SDDE of multipath satellites may be attributed to multipath interference or signal power degradation.

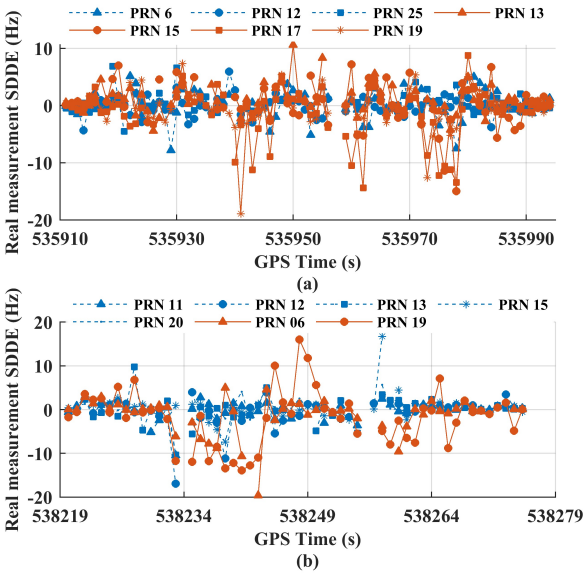

Fig. 7. SDDE values from the real receiver for all visible satellites in (a) scenario 1 and (b) scenario 2. Blue PRN for LOS type, orange for MP type.

TABLE II
Statistical analysis of the SDDE values

Scenario1			
Type	PRNs	STD (Hz)	Satellite elevation (degree)
LOS	25	1.87	15
	12	1.57	30
	6	2.58	33
MP	15	3.93	12
	17	4.51	15
	13	2.55	32
	19	3.49	33
Scenario 2			
Type	PRNs	STD (Hz)	Satellite elevation (degree)
LOS	12	3.46	21
	15	3.31	28
	13	2.88	50
	20	1.34	51
	11	2.31	52
MP	19	6.45	17
	6	4.30	27

The next step is to ensure that the multipath effect is the primary factor contributing to the increased variation in the SDDE of multipath satellites. The impact of the thermal noise is examined based on the satellite elevation angle and the theoretical thermal noise error. Table II furnishes the satellite elevation angles. It is known that for LOS satellites, the received signal strength tends

to be relatively higher when transmitted from satellites positioned at higher elevation angles, and C/N_0 serves as a useful metric for multipath detection [35, 36]. Therefore, the STD of SDDE, derived from the C/N_0 values of the test and reference satellites, is closely correlated with the satellite elevation angle. Comparing the STD of PRNs 15, 17, and 19 in scenario 1, and PRNs 19 and 6 in scenario 2, with the LOS satellites that exhibit similar elevation angles within the same test, an abnormal increase in STD is noted.

Furthermore, the theoretical standard deviation of the SDDE can be calculated based on C/N_0 outputted from the u-blox receiver. Subsequently, the 68–95–99 rule introduced in Section IV.B is applied to test whether the real measurements align with the anticipated theoretical distribution. Algorithm 3 sets B_n and T at 15Hz and 10ms, respectively. Fig. 8. provides examples of the SDDE values and the time-varying 2-sigma values of the thermal noise. For the LOS satellite PRN 12, most results fall within the theoretical 2-sigma intervals. However, for multipath satellite PRN 19, the results exhibit higher oscillation and deviate from conforming to a distribution with a zero mean value.

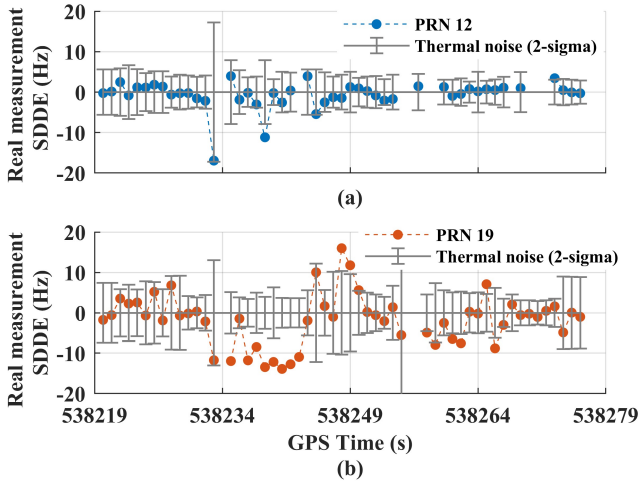

Fig. 8. SDDE values from the real receiver for (a) PRN 12, and (b) PRN 19 in scenario 2. Blue PRN for LOS type, orange for MP type.

Table III summarizes the percentage within the theoretical thermal noise standard deviation for all satellites. Notably, concerning LOS satellites, the average percentages within 1-sigma, 2-sigma, and 3-sigma intervals are 81%, 95% and 99%, respectively. This indicates that the distribution of SDDE for LOS satellites closely adheres to the theoretical distribution, with a stronger concentration around zero. Conversely, results for multipath satellites exhibit greater dispersion. The multipath satellites' average percentages within 1-sigma, 2-sigma, and 3-sigma intervals are 57%, 78% and 88%, respectively. This empirical evidence suggests that the increase in the STD for the multipath satellite may not be attributed to the decline in the received LOS signal strength or the compound signal C/N_0.

In conclusion, the analysis of the SDDE derived from the real receiver indicates that the SDDE of multipath satellites demonstrates more pronounced vibration than LOS satellites, which is likely attributed to multipath interference. In addition, the satellite classification result from the ray-tracing can sometimes be wrong [37].

TABLE III
Distribution of the SDDE values

Type	PRNs	1-sigma (%)	2-sigma (%)	3-sigma (%)
LOS	S1-6	63.1	86.3	95.9
	S1-12	84.3	94.0	100
	S1-25	90.0	98.3	100
	S2-11	88.1	100	100
	S2-12	76.6	95.7	100
	S2-13	80.0	96.0	100
	S2-15	73.3	93.3	97.8
	S2-20	90.2	98.0	100
Average		80.7	95.2	99.2
MP	S1-13	53.3	80.0	92.0
	S1-15	55.1	78.3	89.9
	S1-17	52.5	70.4	85.9
	S1-19	51.2	81.7	90.2
	S2-6	75.5	87.8	89.7
	S2-19	53.7	68.5	81.5
Average		56.9	77.8	88.2

C. Simulated receiver-measured Doppler frequency

Fig. 9. (a) presents an example of simulation results derived from PRN 15 in scenario 1. In this figure, the 'MP Doppler' represents the SDD value of receiver-measured Doppler frequency $\tilde{f}_0$ under multipath reception. 'LOS Doppler' and 'Reflected Doppler' indicate the SDD value derived from the Doppler frequency of the LOS signal f_{LOS} and the reflected signal f_{Refl}, respectively. The calculation of the SDD values follows (32), using the Doppler frequency of PRN 5 as the reference. The subplot within Fig. 9. (a) offers a magnified view specifically around GPS time 535970. Several findings can be drawn from these results. Firstly, the Doppler difference between the LOS and reflected signals becomes significant periodically. This is attributed to the alternating velocity projection onto the signal vector during reciprocal motion. Secondly, although the simulated MP Doppler exhibits a comparable shifting pattern to the LOS Doppler, it fluctuates around this LOS Doppler. The difference between the LOS Doppler and the simulated MP Doppler is denoted as the Doppler multipath error. It is observed that the Doppler multipath error increases in proportion to the Doppler shift of the reflected signal. Finally, the Doppler multipath error is zero when the LOS and reflected signals have identical Doppler values.

Fig. 10. shows an illustrative diagram explaining the MP Doppler oscillation phenomenon. To simplify the analysis, it is assumed that the carrier phase error of the LOS signal remains constant within a short time span, such as from epoch n-1 to n+2. During this interval, the magnitude and direction of the compound signal vector

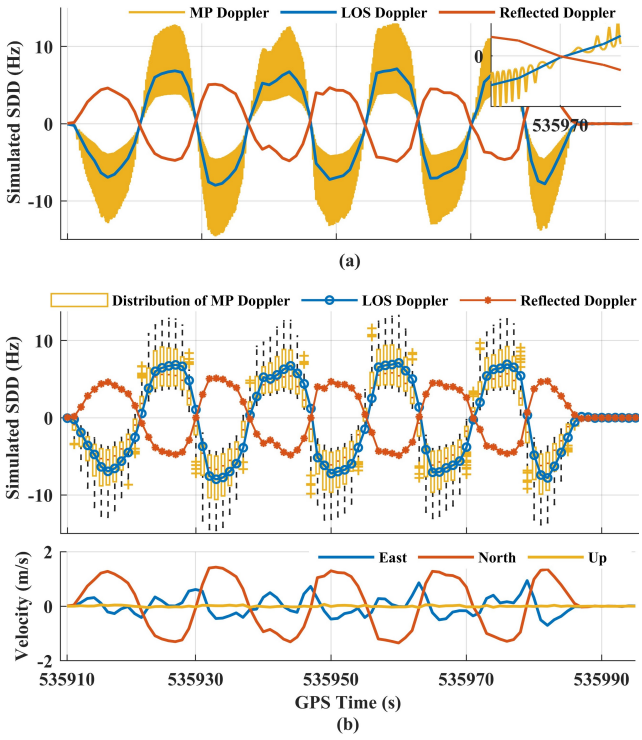

Fig. 9. (a) The simulated SDD values derived from $\tilde{f}_0$, f_{LOS} and f_{Refl} for PRN 15, scenario 1. (b) The box plot of SDD values derived from $\tilde{f}_0$, the SDD values at an output frequency of 1Hz, and the corresponding user velocity in scenario 1.

are influenced by the phase and amplitude of the reflected signals across adjacent epochs. More specifically, the Doppler multipath error increases with the rising phase error change of the reflected signal until the reflected signal vector is perpendicular to the LOS signal vector. In this case, the maximum Doppler multipath error is determined by the radius of the circle of the reflected signal vector. The radius is also recognized as the amplitude of the signal vector. Subsequently, as the carrier phase error of the reflected signal accumulates further, a reversal in the sign of the Doppler multipath error occurs when the compound signal vector rotates in the opposite direction. To summarize, the change in the phase error of the reflected signal significantly impacts the Doppler multipath error, while the maximum attainable Doppler multipath error is contingent upon the amplitude of the reflected signal vector.

It is important to note that the coherent integration time within the receiver tracking loop typically does not exceed 20ms. However, the incorporation rate of GNSS navigation measurements from a commercial receiver is generally 1Hz [1]. Additionally, due to the uncertain updates of the tracking loop and carrier phase tracking in the commercial receiver, the precise Doppler frequency output remains unpredictable for the proposed FLL simulator. To enhance the realism of the simulation, aligning the output rate with the commercial receiver's frequency is necessary. Fig. 9. (b) presents the box plot of the simulated MP Doppler, where each box exhibits a

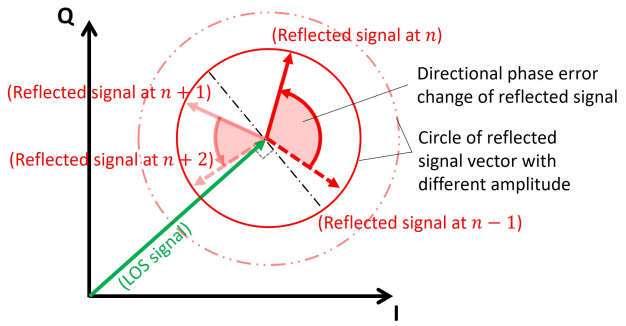

Fig. 10. Illustration of the receiver Doppler measurement oscillation.

distribution derived from 100 epochs. It is observed that the simulated MP Doppler exhibits a skewed distribution within each second, with the majority of samples concentrated on the side closer to the LOS Doppler. Furthermore, considering the minimum and maximum values of the boxes as the error bars of the simulated MP Doppler, these bars delineate the maximum and minimum Doppler values encompassed within one second. Consequently, the error bars serve to describe the potential Doppler measurement values in the presence of multipath effects. It was observed that the error bars expand as user velocity and frequency shift of the reflected signal increase.

D. Experimental validation of the simulator

To validate the effectiveness of this simulator, the simulation results are compared with the commercial receiver output. The Pearson correlation coefficient is utilized to describe the similarity between the simulation results and real receiver measurement, which is expressed as [38]

$$\begin{aligned}\rho(\boldsymbol{a},\boldsymbol{b}) &= \frac{(\boldsymbol{a}-\bar{\boldsymbol{a}})\cdot(\boldsymbol{b}-\bar{\boldsymbol{b}})}{\|\boldsymbol{a}-\bar{\boldsymbol{a}}\|\times\|\boldsymbol{b}-\bar{\boldsymbol{b}}\|} \\ &= \frac{\sum_{i=1}^{k}(a_i-\bar{a})(b_i-\bar{b})}{\sqrt{\sum_{i=1}^{k}(a_i-\bar{a})^2}\sqrt{\sum_{i=1}^{k}(b_i-\bar{b})^2}}\end{aligned} \tag{36}$$

where $\bar{\boldsymbol{a}} = \frac{1}{k}\sum_{i=1}^{k} a_i$ and analogously for $\bar{b}$. The closer the Pearson correlation coefficient is to 1, the better the match between the two datasets. In the following sections, the Pearson correlation coefficient is referred to as the 'similarity' between the simulation output and the real measurements.

Due to the limited knowledge of the carrier phase, the simulation generates an output frequency of 1Hz, exhibiting variability in each attempt. For each satellite, 10,000 attempts were conducted to compare the simulator output with the real measurements. Table IV shows the similarity of MP Doppler and LOS Doppler to the real Doppler measurement. For all the satellites, the average maximum similarity of the MP Doppler can reach around 81%, showing that our simulator predicts the receiver-measured Doppler frequency with satisfactory accuracy.

The mean similarity of the MP Doppler is similar to that of the LOS Doppler. This is because the LOS Doppler is, essentially, a possible output of the simulated MP Doppler, situated within the concentrated region of the distribution and proximate to the median. Comparing the similarity achieved by the simulated MP Doppler with that of the LOS Doppler, there is a potential enhancement of up to approximately 10% in simulation accuracy for most PRNs. Notably, for PRN 13, the maximum similarity achieved by the MP Doppler is comparable to that of the LOS Doppler. This suggests that the signals received in the commercial receiver from PRN 13 might solely contain the LOS signal, while our simulator, due to the wrong classification of the ray-tracing algorithm, simulates the Doppler frequency considering multipath reception.

TABLE IV
Similarity to real Doppler measurement

PRNs	Simulator output			LOS Doppler (%)
	max (%)	mean (%)	min (%)	
S1-13	88.4	81.1	71.4	87.6
S1-15	79.1	64.4	47.2	69.4
S1-17	74.7	61.8	47.5	62.1
S1-19	81.1	73.9	63.3	74.9
S2-6	84.3	76.3	67.2	77.9
S2-19	79.3	65.7	52.8	65.6

Fig. 11. and Fig. 12. provide the simulator output for all MP satellites with the highest similarity and the real Doppler measurement in scenarios 1 and 2, respectively. There are several potential reasons for the simulation inaccuracy and the unexpected fluctuations observed in the real Doppler measurements. First, the carrier phase error in the real receiver might be influenced by updates in the PLL, resulting in an unpredictable alteration in the output of the FLL discriminator, thereby leading to rapid jumps in the Doppler measurements. Second, during real experiments, unpredictable changes in the satellite type might occur. Third, variations in the power of the reflected and LOS signals in real experiments might occur due to changes in the materials of the reflector surfaces as well as potential blockages caused by pedestrians and trees. Moreover, it's important to note that the proposed simulator operates in a noise-free environment. However, in real-world scenarios, the presence of thermal noise can exert a substantial impact on the receiver's tracking accuracy. Lastly, the code tracking errors affect the signal vector amplitude, thereby impacting real receiver Doppler measurements.

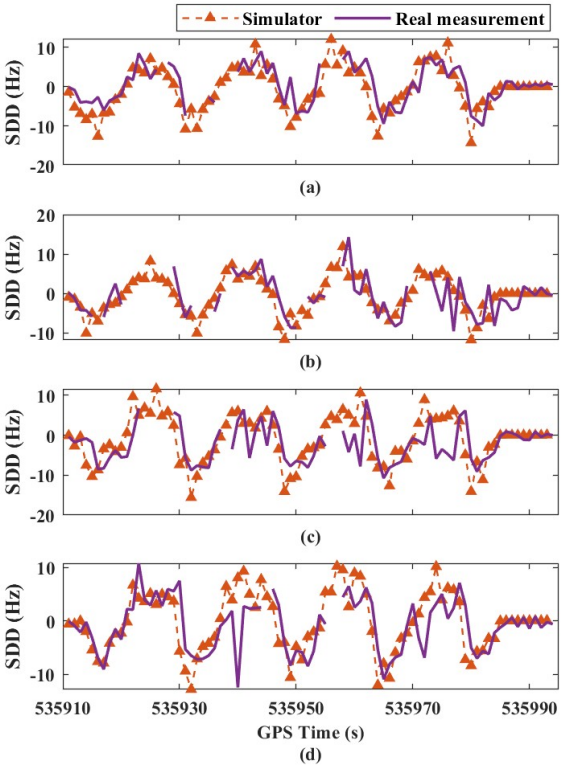

Fig. 11. The comparison between simulated SDD of the MP Doppler output and SDD of the real measurement of (a) PRN 13, (b) PRN 15, (c) PRN 17, and (d) PRN 19 in scenario 1.

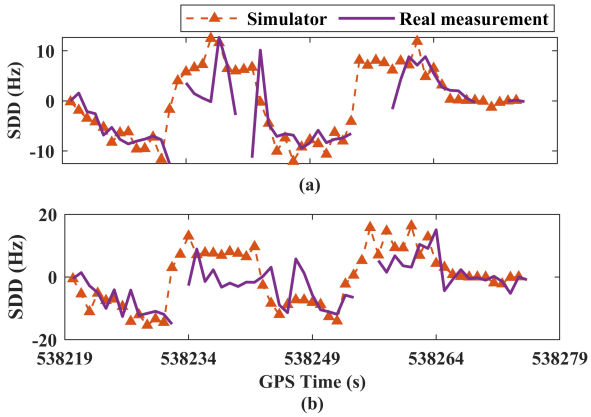

Fig. 12. The comparison between simulated SDD of the MP Doppler output and SDD of the real measurement of (a) PRN 6 and (b) PRN 19 in scenario 2.

E. Simulation of more scenarios

This section simulates more scenarios with higher user velocity magnitudes to quantify the Doppler multipath error and receiver velocity estimation errors in urban areas. During each simulation test, the user receiver moves at a constant speed and direction for one second. The simulation environment and time are identical to those in scenario 1, as depicted in Fig. 6 (a). The detailed settings for the unchanged variables are provided in Table V.

Fig. 13. depicts the simulated maximum Doppler multipath error and the corresponding pseudorange rate error for PRN 13 of scenario 1, considering the varying user velocity and R/D power ratios. The results show that multipath-induced errors increase with higher user velocities, reaching a maximum when the user velocity is approximately 5m/s. This can be explained by the error envelopes shown in Fig. 3 (a), as increasing user

TABLE V
Settings for simulation tests

Ground truth location	22.29306°N, 114.17423°E
GPS week/seconds	2270/535923-535924
Satellite	PRN 13 for Fig.13 PRNs 5, 6, 12, 13, 15, 17, 19, 25 for Fig.14
User velocity direction	Perpendicular to the building surface

velocity leads to a greater frequency shift of the reflected signal, resulting in larger multipath-induced errors. The negligible error observed at around 15m/s may be due to the compound signal's carrier phase error approaching the detection limit of the discriminator. This also aligns with the theoretical envelopes, which show zero error in the receiver measurement when the normalized frequency shift is 0.5. As user velocity and frequency shift continue to increase, a lower peak of the receiver measurement error is observed. Additionally, the receiver measurement errors increase faster and attain higher maximum values when the reflected signal is stronger.

Comparison between Fig. 13 and Fig. 3 (a) shows that the simulated multipath-induced error in Fig. 13 is larger due to Doppler measurement oscillation during the one-second simulation period. However, the relationship between multipath-induced error and Doppler frequency shift remains consistent. In conclusion, the simulated error in the realistic FLL simulator aligns with the theoretical error envelope in Fig. 3 (a).

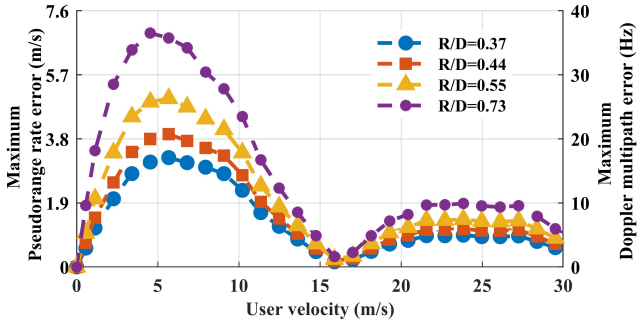

Fig. 13. Simulation of the maximum pseudorange rate error and Doppler multipath error with increasing user velocity for PRN 13, scenario 1 and $T = 10$ms.

The user velocity and user clock bias can be estimated using the LS method [25]. The horizontal receiver velocity estimation error can be written as

$$v_{err} = \sqrt{(v_E - v_{E,GT})^2 + (v_N - v_{N,GT})^2} \qquad (37)$$

where v_E and v_N represent the receiver-estimated velocities in the east and north directions, respectively. $v_{E,GT}$ and $v_{N,GT}$ represent the ground true receiver velocities in the east and north directions, respectively. Following Algorithm 2, the simulation results of the receiver velocity estimation error are depicted in Fig. 14. The simulation settings are shown in Table V, and the skyplot is the same as that shown in Fig. 6 (a). For each sample of the simulation test, the Doppler multipath error is randomly selected from the simulated distribution of the Doppler multipath error over one second. Fig. 14 shows that the distribution

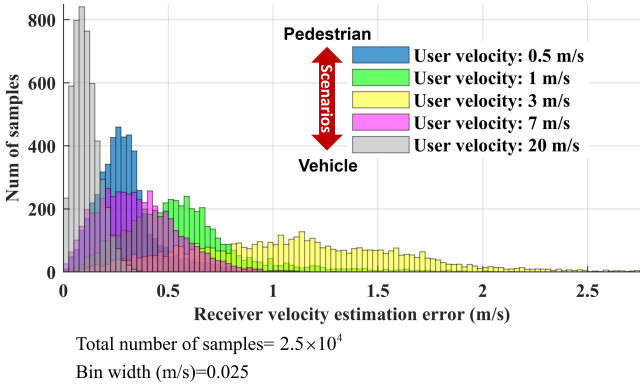

Fig. 14. The simulated horizontal receiver velocity estimation error due to the multipath interference with the R/D power ratios of the multipath satellites ranges from 0.4 to 0.5 and $T = 10$ms.

of the receiver's velocity estimation error adheres to a skewed distribution, becoming more dispersed as user velocity increases from 0.5m/s to 3m/s. This phenomenon can be explained by the theoretical envelope in Fig. 3 (a), as higher user velocity leads to larger frequency shifts in the reflected signals, which in turn increases pseudorange rate errors for the multipath channels, resulting in larger receiver velocity estimation errors. Additionally, Fig. 14 shows that the receiver velocity estimation error diminishes as the user velocity increases further, such as at 7m/s and 20m/s. According to Fig. 3 (a), when most reflected signals exhibit large frequency shifts, the amplitude of the reflected signal vectors is significantly degraded, resulting in reduced Doppler and velocity measurement errors.

In conclusion, the performance of Doppler multipath error and velocity estimation error varies across different scenarios, contingent upon the geometric relationships between satellites, reflection points, and receivers. Our simulator exhibits satisfactory accuracy in estimating receiver Doppler measurements and demonstrates the capability to forecast receiver velocity estimation errors in urban environments.

VI. CONCLUSION

This paper analyzes the Doppler measurement performance of a typical FLL under multipath interference. The Doppler multipath error and pseudorange rate error envelopes are illustrated in a specific scenario. A single-difference Doppler error model (SDDE) is introduced to analyze the multipath interference and noise impact on the real Doppler measurement. The real experiment results show that the SDDE value of the possible multipath satellites demonstrates more pronounced vibration compared with the LOS satellites. A realistic simulator is introduced to visualize the receiver Doppler measurement performance in urban environments. This simulator combines the typical receiver feedback tracking loop with ray-tracing and is able to quantify the possible Doppler measurement error. The reliability of the proposed FLL

simulator is validated by calculating the similarity between the simulated Doppler frequency and the real Doppler frequency outputted from the commercial receiver. The simulation similarity is able to achieve around 81%. We further characterize the Doppler multipath error and receiver velocity estimation error with varying user dynamics. The results show that multipath-induced errors increase with a larger reflected signal frequency shift and higher reflected signal power, but the error decreases when the frequency shift of the reflected signal is significantly large.

In the future, the performance of Doppler measurements across different receiver types may be simulated through the application of different navigation filters. This effort aims to offer predictions of Doppler measurement errors across different practical applications using our simulator. Enhanced simulation accuracy could be achieved by incorporating the carrier phase tracking loop and the code tracking loop. Additionally, forthcoming real-world experiments will involve higher user velocities to discuss Doppler multipath errors in vehicular applications. Moreover, future research will investigate multipath interference on receiver velocimetry and positioning accuracy. These efforts seek to provide valuable insights that could significantly contribute to augmenting the reliability of GNSS navigation applications.

APPENDIX

A. Correlation and discriminator

The I-channel output in (6) mainly consists of the high-frequency and low-frequency output components as

$$\begin{aligned}
&i_p(t)\\
&= [\sqrt{2C_{LOS}}D(t-\tau_{LOS})x(t-\tau_{LOS})\sin(\omega_{LOS}t+\vartheta_{LOS})\\
&+ \sqrt{2C_{Refl}}D(t-\tau_{Refl})x(t-\tau_{Refl})\sin(\omega_{Refl}t+\vartheta_{Refl})]\\
&\times \sqrt{2}x(t-\tau_0)\sin(\omega_0 t+\vartheta_0)\\
&= -\sqrt{C_{LOS}}D(t-\tau_{LOS})x(t-\tau_{LOS})x(t-\tau_0)\\
&\times [\cos((\omega_{LOS}+\omega_0)t+\vartheta_{LOS}+\vartheta_0)\\
&- \cos((\omega_{LOS}-\omega_0)t+\vartheta_{LOS}-\vartheta_0)]\\
&- \sqrt{C_{Refl}}D(t-\tau_{Refl})x(t-\tau_{Refl})x(t-\tau_0)\\
&\times [\cos((\omega_{Refl}+\omega_0)t+\vartheta_{Refl}+\vartheta_0)\\
&- \cos((\omega_{Refl}-\omega_0)t+\vartheta_{Refl}-\vartheta_0)]
\end{aligned} \tag{A.1}$$

For (18) and (19), the detailed calculations are

$$\begin{aligned}
P_{dot} &= I_p(n)I_p(n-1) + Q_p(n)Q_p(n-1)\\
&= [A_{LOS,n}\cos(\phi_{LOS,n}) + A_{Refl,n}\cos(\phi_{Refl,n})]\\
&\quad [A_{LOS,n-1}\cos(\phi_{LOS,n-1}) + A_{Refl,n-1}\cos(\phi_{Refl,n-1})]\\
&\quad + [A_{LOS,n}\sin(\phi_{LOS,n}) + A_{Refl,n}\sin(\phi_{Refl,n})]\\
&\quad [A_{LOS,n-1}\sin(\phi_{LOS,n-1}) + A_{Refl,n-1}\sin(\phi_{Refl,n-1})]\\
&= A_{LOS,n}A_{LOS,n-1}\cos(\phi_{LOS,n}-\phi_{LOS,n-1})\\
&\quad + A_{LOS,n}A_{Refl,n-1}\cos(\phi_{LOS,n}-\phi_{Refl,n-1})\\
&\quad + A_{Refl,n}A_{LOS,n-1}\cos(\phi_{Refl,n}-\phi_{LOS,n-1})\\
&\quad + A_{Refl,n}A_{Refl,n-1}\cos(\phi_{Refl,n}-\phi_{Refl,n-1})
\end{aligned} \tag{A.2}$$

$$\begin{aligned}
P_{cross} &= Q_p(n)I_p(n-1) - I_p(n)Q_p(n-1)\\
&= [A_{LOS,n}\sin(\phi_{LOS,n}) + A_{Refl,n}\sin(\phi_{Refl,n})]\\
&\quad [A_{LOS,n-1}\cos(\phi_{LOS,n-1}) + A_{Refl,n-1}\cos(\phi_{Refl,n-1})]\\
&\quad - [A_{LOS,n}\cos(\phi_{LOS,n}) + A_{Refl,n}\cos(\phi_{Refl,n})]\\
&\quad [A_{LOS,n-1}\sin(\phi_{LOS,n-1}) + A_{Refl,n-1}\sin(\phi_{Refl,n-1})]\\
&= A_{LOS,n}A_{LOS,n-1}\sin(\phi_{LOS,n}-\phi_{LOS,n-1})\\
&\quad + A_{LOS,n}A_{Refl,n-1}\sin(\phi_{LOS,n}-\phi_{Refl,n-1})\\
&\quad + A_{Refl,n}A_{LOS,n-1}\sin(\phi_{Refl,n}-\phi_{LOS,n-1})\\
&\quad + A_{Refl,n}A_{Refl,n-1}\sin(\phi_{Refl,n}-\phi_{Refl,n-1})
\end{aligned} \tag{A.3}$$

B. The pseudorange rate error and Doppler multipath error envelopes

(24) can be simplified as

$$\dot{\rho}_{error,n} = \frac{\lambda}{2\pi T}\arctan\left(\frac{\sin(x)}{\alpha+\cos(x)}\right) \tag{B.1}$$

where

$$\alpha = \frac{A_{LOS,n}}{A_{Refl,n}}$$
$$x = 2\pi f_{shift,n}T + \vartheta_{shift,n}$$

Define the inner function as

$$y = \frac{\sin(x)}{\alpha+\cos(x)} \tag{B.2}$$

Take the derivative of the function y, the maximum and minimum values of the function y can be found when $\cos(x) = -1/\alpha$. Therefore, the pseudorange rate error reaches extremes

$$\dot{\rho}^{\max}_{error,n} = \frac{\lambda}{2\pi T}\arctan\left(\frac{1}{\sqrt{\alpha^2-1}}\right) \tag{B.3}$$

$$\dot{\rho}^{\min}_{error,n} = \frac{\lambda}{2\pi T}\arctan\left(-\frac{1}{\sqrt{\alpha^2-1}}\right) \tag{B.4}$$

According to (25) and (26), α can be written as

$$\alpha = \frac{\sqrt{C_{LOS,n}}R(\Delta\tau_{LOS,n})}{\sqrt{C_{Refl,n}}R(\Delta\tau_{Refl,n})\mathrm{sinc}(f_{shift,n}T)} \tag{B.5}$$

Therefore, the pseudorange rate error envelope is nonlinear with respect to changes in $f_{shift,n}$. Generally, the pseudorange rate error decreases with a larger coherent integration time and a lower reflected signal amplitude.

REFERENCES

[1] E. D. Kaplan and C. Hegarty, *Understanding GPS/GNSS: Principles and Applications*, 3rd ed. Boston, MA, USA: Artech House, 2017.

[2] P. D. Groves, Z. Jiang, M. Rudi, and P. Strode, "A portfolio approach to NLOS and multipath mitigation in dense urban areas," in *Proc. 26th Int. Tech. Meet. Satellite Division Inst. Navigat. (ION GNSS)*, 2013, pp. 3231–3247.

[3] N. Kbayer and M. Sahmoudi, "Performances analysis of GNSS NLOS bias correction in urban environment using a three-dimensional city model and

GNSS simulator," *IEEE Trans. Aerosp. Electron. Syst.*, vol. 54, no. 4, pp. 1799–1814, 2018.

[4] S. K. Kalyanaraman, M. S. Braasch, and J. M. Kelly, "Code tracking architecture influence on GPS carrier multipath," *IEEE Trans. Aerosp. Electron. Syst.*, vol. 42, no. 2, pp. 548–561, 2006.

[5] C. Lubeigt, L. Ortega, J. Vilà-Valls, L. Lestarquit, and E. Chaumette, "Clean-to-composite bound ratio: A multipath criterion for GNSS signal design and analysis," *IEEE Trans. Aerosp. Electron. Syst.*, vol. 58, no. 6, pp. 5412–5424, 2022.

[6] J. M. Kelly, M. S. Braasch, and M. F. DiBenedetto, "Characterization of the effects of high multipath phase rates in GPS," *GPS Solutions*, vol. 7, pp. 5–15, 2003.

[7] R. Yang, X. Zhan, W. Chen, and Y. Li, "An iterative filter for FLL-Assisted-PLL carrier tracking at low C/N_0 and high dynamic conditions," *IEEE Trans. Aerosp. Electron. Syst.*, vol. 58, no. 1, pp. 275–289, 2022.

[8] N. Qian, G. Chang, J. Gao, C. Pan, L. Yang, F. Li, H. Yu, and J. Bu, "Vehicle's instantaneous velocity reconstruction by combining GNSS Doppler and carrier phase measurements through Tikhonov regularized kernel learning," *IEEE Trans. Veh. Technol.*, vol. 70, no. 5, pp. 4190–4202, 2021.

[9] N. Kubo, "Advantage of velocity measurements on instantaneous RTK positioning," *GPS solutions*, vol. 13, no. 4, pp. 271–280, 2009.

[10] M. Irsigler, "Characterization of multipath phase rates in different multipath environments," *GPS solutions*, vol. 14, no. 4, pp. 305–317, 2010.

[11] P. Xie and M. G. Petovello, "Measuring GNSS multipath distributions in urban canyon environments," *IEEE Trans. Instrum. Meas.*, vol. 64, no. 2, pp. 366–377, 2014.

[12] X. Chen, Y. J. Morton, W. Yu, and T.-K. Truong, "GPS L1CA/BDS B1I multipath channel measurements and modeling for dynamic land vehicle in Shanghai dense urban area," *IEEE Trans. Veh. Technol.*, vol. 69, no. 12, pp. 14 247–14 263, 2020.

[13] N. S. Gowdayyanadoddi, J. T. Curran, A. Broumandan, and G. Lachapelle, "A ray-tracing technique to characterize GPS multipath in the frequency domain." *Int. J. Navigation Observation*, vol. 2015, 2015, Art. no. 983124.

[14] G. Brodin and P. Daly, "GNSS code and carrier tracking in the presence of multipath," *Int. J. Satell. Commun.*, vol. 15, no. 1, pp. 25–34, 1997.

[15] P. R. Strode and P. D. Groves, "GNSS multipath detection using three-frequency signal-to-noise measurements," *GPS solutions*, vol. 20, pp. 399–412, 2016.

[16] N. Jardak, A. Vervisch-Picois, and N. Samama, "Multipath insensitive Delay Lock Loop in GNSS receivers," *IEEE Trans. Aerosp. Electron. Syst.*, vol. 47, no. 4, pp. 2590–2609, 2011.

[17] Y. Wang and Z. Huang, "MEDLL on-strobe correlator: a combined anti-multipath technique for GNSS signal tracking," *J. Navigation*, vol. 73, no. 3, pp. 658–677, 2020.

[18] C. Siebert, A. Konovaltsev, and M. Meurer, "Development and validation of a multipath mitigation technique using multi-correlator structures," *Navig. J. Inst. Navig.*, vol. 70, no. 4, 2023.

[19] L. Xu and J. Rife, "Modeling multipath effects on frequency locked loops," in *Proc. Inst. Navigat. Int. Tech. Meet. (ION ITM)*, San Diego, CA, USA, 2020, pp. 698–712.

[20] S. Li, R. Yang, and X. Zhan, "Characterization of multi-band GNSS multipath in urban canyons using the 3D ray-tracing method," *GPS Solutions*, vol. 28, no. 1, p. 49, 2024.

[21] J. Fang, L. Zhang, G. Zhang, B. Xu, and L.-T. Hsu, "Modeling and validation of GNSS multipath-induced Doppler tracking error," in *Proc. Inst. Navigat. Int. Tech. Meet. (ION ITM)*, Long Beach, CA, USA, 2024, pp. 931–940.

[22] Z. Luo, J. Ding, L. Zhao *et al.*, "Adaptive gain control method of a phase-locked loop for GNSS carrier signal tracking," *Int. J. Antennas Propag.*, vol. 2018, 2018.

[23] J. T. Curran, G. Lachapelle, and C. C. Murphy, "Digital GNSS PLL design conditioned on thermal and oscillator phase noise," *IEEE Trans. Aerosp. Electron. Syst.*, vol. 48, no. 1, pp. 180–196, 2012.

[24] L. Lau and P. Cross, "Development and testing of a new ray-tracing approach to GNSS carrier-phase multipath modelling," *J. Geodesy*, vol. 81, pp. 713–732, 2007.

[25] P. Misra and P. Enge, *Global positioning system: signals, measurements, and performance*, 2nd ed. New York, NY, USA: Ganga-Jamuna Press, 2006.

[26] B. W. Parkinson and J. J. Spilker, *Global positioning system: Theory and Applications Volume I*. Washington, DC, USA: AIAA, 1996, pp. 379–385.

[27] M. Lashley, D. M. Bevly, and J. Y. Hung, "Performance analysis of vector tracking algorithms for weak GPS signals in high dynamics," *IEEE J. Sel. Topics Signal Process.*, vol. 3, no. 4, pp. 661–673, 2009.

[28] J.-H. WON, D. Dötterböck, and B. Eissfeller, "Performance comparison of different forms of Kalman filter approaches for a vector-based GNSS signal tracking loop," *Navigation*, vol. 57, no. 3, pp. 185–199, 2010.

[29] B. Xu, Q. Jia, and L.-T. Hsu, "Vector tracking loop-based GNSS NLOS detection and correction: Algorithm design and performance analysis," *IEEE Trans. Instrum. Meas.*, vol. 69, no. 7, pp. 4604–4619, 2019.

[30] R. Yang, K.-V. Ling, E.-K. Poh, and Y. Morton, "Generalized GNSS signal carrier tracking: Part I—Modeling and analysis," *IEEE Trans. Aerosp. Electron. Syst.*, vol. 53, no. 4, pp. 1781–1797, 2017.

[31] Z. Yao and M. Lu, *Next-Generation GNSS Signal Design*. Berlin, Germany: Springer, 2021.
[32] G. Zhang, B. Xu, H.-F. Ng, and L.-T. Hsu, "GNSS RUMS: GNSS realistic urban multiagent simulator for collaborative positioning research," *Remote Sens.*, vol. 13, no. 4, p. 544, 2021.
[33] F. Huang, W. Wen, J. Zhang, and L.-T. Hsu, "Point wise or feature wise? A benchmark comparison of publicly available Lidar odometry algorithms in urban canyons," *IEEE Intell. Transp. Syst. Mag.*, vol. 14, no. 6, pp. 155–173, 2022.
[34] L. Zhang, H.-F. Ng, G. Zhang, and L.-T. Hsu, "3D mapping aided GNSS positioning using Doppler frequency for urban areas," in *Proc. 36th Int. Tech. Meet. Satellite Division Inst. Navigat. (ION GNSS+ 2023)*, Denver, CO, USA, 2023, pp. 2897–2905.
[35] N. Kubo, K. Kobayashi, and R. Furukawa, "GNSS multipath detection using continuous time-series C/N0," *Sensors*, vol. 20, no. 14, p. 4059, 2020.
[36] J. B.-Y. Tsui, *Fundamentals of global positioning system receivers: a software approach*. New York: Wiley, 2005.
[37] H.-F. Ng, G. Zhang, and L.-T. Hsu, "A computation effective range-based 3D mapping aided GNSS with NLOS correction method," *J. Navigat.*, vol. 73, no. 6, pp. 1202–1222, 2020.
[38] K. Pearson, "Note on regression and inheritance in the case of two parents," *Proc. Roy. Soc. London*, vol. 58, no. 347-352, pp. 240–242, 1895.

Jingxiaotao Fang received her bachelor's degree in the Department of Aeronautical and Aviation Engineering from The Hong Kong Polytechnic University in 2022. She is currently a Ph.D. student at the Department of Aeronautical and Aviation Engineering, The Hong Kong Polytechnic University, Hong Kong. Her research interests include GNSS signal processing for GNSS navigation accuracy and security.

Liyuan Zhang received his B.E. degree in electronic and information engineering from the Chongqing University of Posts and Telecommunications, China. He received his M.S. degree in electronic and communication engineering from Beihang University, China. He is currently a Ph.D. student in the Department of Aeronautical and Aviation Engineering, The Hong Kong Polytechnic University. His research interests include 3D mapping-aided GNSS velocity estimation in urban canyons.

Guohao Zhang received his bachelor's degree in mechanical engineering and automation from University of Science and Technology Beijing, China. He received his master's degree in Mechanical Engineering and his Ph.D. degree in Aeronautical and Aviation Engineering, Hong Kong Polytechnic University. He is currently a research assistant professor at Department of Aeronautical and Aviation Engineering of Hong Kong Polytechnic University. He won the Best Presentation Award in 2018 and the ION GNSS+ Student Paper Award in 2019 from the Institute of Navigation (ION). His research interests include GNSS urban positioning, collaborative positioning, machine learning aided GNSS, signal propagation, and multi-sensor integrated navigation.

Bing Xu (Member, IEEE) is currently an Assistant Professor with the Department of Aeronautical and Aviation Engineering, The Hong Kong Polytechnic University, Hong Kong. Prior to the current post, he was Postdoctoral Fellow and Research Assistant Professor with the same institute. He received his BEng and Ph.D. degrees from Nanjing University of Science and Technology in 2012 and 2018, respectively. His research focuses on GNSS signal processing and its applications to multipath and spoofing problems. He is also interested in LEO navigation and cellular signal positioning.

Li-Ta Hsu (Senior Member, IEEE) received the B.S. and Ph.D. degrees in aeronautics and astronautics from National Cheng Kung University, Tainan, Taiwan, in 2007 and 2013, respectively. He was a Visiting Researcher with the Faculty of Engineering, University College London and Tokyo University of Marine Science and Technology, in 2012 and 2013, respectively. He was a JSPS Postdoctoral Fellow with The University of Tokyo, from 2014 to 2016. He is currently an Associate Professor with the Department of Aeronautical and Aviation Engineering, Hong Kong Polytechnic University, Hong Kong.

Dr. Hsu is Limin Endowed Young Scholar in Aerospace Navigation. He is an Associate Fellow with the Royal Institute of Navigation. He is currently a Member of the Institute of Navigation and serves as a Member of the editorial board and a Reviewer in professional journals related to navigation and global navigation satellite system.